Int. J. Microgravity Sci. Appl., **35** (3) (2018) 350305
DOI: 10.15011//jasma.35.350305

IIII Original Paper IIII

Nucleation Processes of Cosmic Dust Investigated by Microgravity Experiments using an Airplane

Yuki KIMURA[1], Shinnosuke ISHIZUKA[1,6], Sašo ŠTURM[2], Kyoko K. TANAKA[1,7], Tomoya YAMAZAKI[1], Fumiaki SAITO[1], Yosuke SATOH[1], Katsuo TSUKAMOTO[3] and Yuko INATOMI[4,5]

Abstract

Cosmic dust, which is composed of nanometer-sized particles and is ubiquitously distributed in the universe, is formed in a gas outflow from evolved stars under a microgravity environment. Its formation processes have been studied on the basis of knowledge obtained under the 1 G environment on Earth and is thus not fully understood under realistic conditions. To better understand the process, here, we performed nucleation experiments of dust analogs under a microgravity environment. We show the details of our experiments using an aircraft including results of in-situ observation employing an interferometer and ex-situ transmission electron microscopy to reveal the difficulty of nucleation and variability of nucleation processes. Of particular note is the size distribution of the produced particle, which was monotonical in microgravity experiments against a double peak for particles produced in the laboratory. Under a microgravity environment, nucleation tends to suppress because of smaller density fluctuation due to convection free and less turbulence due to smaller Reynolds number which gives atoms/molecules (particles) smaller chance to collide with each other for nucleation (coagulation).

Keyword(s): In-situ observation, Interferometer, Infrared, Nanoparticle, Dust.
Received 10 May 2018, accepted 17 July 2018, published 31 July 2018.

1. Introduction

There is a large hindrance to form a solid material from both vapor and liquid phases. For example, although the melting point of ice is well known to be 0°C, water does not freeze to form ice at 0°C at atmospheric pressure. To form ice from water, water molecules must align periodically in three dimensions by undergoing a process known as nucleation. When molecules begin to arrange in a crystalline lattice, the newly created surface has a certain disadvantage regarding free energy. Thus, nucleation must overcome a large potential barrier for continuous growth. A molecule located on the topmost surface of a solid material easily desorbs to a mother phase. Continuous growth of a crystal requires a larger amount of bulk free energy, which becomes larger with the degree of supercooling. A crystal with a smaller amount of surface free energy nucleates under a relatively smaller degree of supercooling. In addition, larger sticking probability promotes efficient nucleation. A relationship exists between the waiting time for nucleation (incubation time) and the degree of supercooling; larger supercooling shortens the waiting time for nucleation. For example, in case of water, the waiting time becomes almost zero at about -40°C[1)].

Similarly, cosmic dust particles, referred to here as dust, do not nucleate even when a gas cools to a temperature of thermal equilibrium for a mineral[2)]. Although the required degree of supersaturation, which corresponds to supercooling for water, is unknown for the formation of dust, it depends strongly on the polymorph of a mineral. This is because the surface free energy of a metastable crystal and amorphous phase is smaller than that of its stable crystal, which suggests easier formation than that for a stable crystal[3)]. Therefore, nucleation can occur at a smaller supersaturation level if the molecule finds a more favorable nucleation route in energetically.

Referred to as presolar dust, very old grains that formed more than 4.6 billion year ago can be found in terrestrial samples such as meteorites and interplanetary dust particles. Isotopic analysis and theoretical approaches suggest that dust, which is the building block of solar system bodies, formed in a supernovae remnant and a gas outflow from a red-giant star. We cannot fully understand the formation process of dust despite the quite simple

1 Institute of Low Temperature Science, Hokkaido University, Kita-19, Nishi-8, Kita-ku, Sapporo, 060-0819, Japan.
2 Jožef Stefan Institute, Department for Nanostructured Materials, Jamova 39, 1000 Ljubljana, Slovenia.
3 Department of Earth Science, Graduate School of Science, Tohoku University, Sendai, Miyagi 980-8578, Japan.
4 Japan Aerospace Exploration Agency, Institute of Space and Astronautical Science, 3-1-1 Yoshinodai, Chuo-ku, Sagamihara, Kanagawa 252-5210, Japan.
5 SOKENDAI (The Graduate University for Advanced Studies), School of Physical Sciences, 3-1-1, Yoshinodai, Chuo-ku, Sagamihara, Kanagawa 252-5210, Japan.
6 Present address: National Institute for Environmental Studies, Onogawa 16-2, Tsukuba, Ibaraki 305-0053, Japan.
7 Present address: Astronomical Institute, Graduate School of Science, Tohoku University, 6-3, Aramaki Aza Aoba, Aoba-ku, Sendai, Miyagi 980-8578, Japan.
(E-mail: E-Mail: ykimura@lowtem.hokudai.ac.jp)

process of solid particle formation by agglomeration of atoms or molecules from a gas. However, we believe that the main reason is the physical properties of nanoparticles. The growth of dust progresses in a mesoscopic size scale from 0.1 nm for atoms/molecules to 100 nm for the typical size of dust. The physical properties of a particle with a mesoscopic size are different from that of bulk materials and are also not explained by the fundamental physics of atoms and molecules. Nevertheless, dust formation processes have been studied based mainly on thermodynamics and solid-state physics at the macroscopic scale. It is widely accepted that melting point of nanoparticles is decreasing with size decreases and finally to be half of that of bulk, and the diffusion coefficient can be more than nine orders larger than that of bulk[4–7].

Recently, we demonstrated that two physical properties, surface free energy and sticking probability, most strongly affect the nucleation process[8]. Uncertainties in these two physical quantities create difficulties on the expectation using a nucleation model. Generally, the surface free energy of bulk material is used, and the sticking probability is assumed to be unity for theoretical modeling of nucleation. To determine these physical parameters of dust analogs with a similar size and temperature environment, we have performed a nucleation experiment using interferometry[8–11]. The nucleation temperature and concentration (partial pressure) of a condensing gas from a supersaturated vapor can be determined simultaneously using our method of dual-color interferometry[12]. Based on these nucleation conditions and the timescale for gas cooling, which corresponds to an incubation time for nucleation, two physical parameters can be determined.

Critical questions that remain largely unanswered are related to the phenomena, which control the overcoming of the nucleation barrier and the nucleation progression mechanisms. We attempt in this study to provide a part of an answer to these questions by conducting nucleation experiments using originally designed experimental systems under microgravity conditions.

2. Characteristics of Microgravity Experiments using an Aircraft

We performed microgravity experiments using sounding rockets S-520 28 for understanding a form of iron in the universe and S-520 30 for understanding the nucleation processes of oxide dust around evolved stars in December 2012 and September 2015, respectively[12]. Sounding rockets provide a high-quality microgravity environment on the order of 10^{-4} G for several minutes and therefore offer an irreplaceable opportunity to duplicate dust formation processes. In the case of the Japanese sounding rocket, the whole experimental setup is designed so that both the experimental systems and samples cannot be recovered because the rocket is meant to free fall in the Pacific Ocean approximately 300 km from the coast line. In addition, the experimental setup is highly restricted, for example, confine in a rather small volume; consequently, relatively longer preparation time is spent for the design and construction of the custom made experimental system and for the series of ground testing.

In the case of experiments using an aircraft, the duration and the quality of microgravity are only ~20 s and 10^{-1} – 10^{-2} G, respectively, but the produced samples can be recovered for further study by various ex-situ analytical methods. Moreover, experimental systems are reusable, and about 12 parabolas per day are possible for 4 days in one campaign. Therefore, we can modify the experimental system and condition of every flight. In our study, recovering the sample allowed us to analyze the produced samples for determination of number density, size, and crystalline structure. These data are crucial to determining the origin of the determined physical properties. For these reasons, airplane experiments are also suitable for confirming rocket experiments and testing for future projects. Thus, a microgravity experiment using an aircraft has several advantages over that using a sounding rocket.

We performed microgravity experiments using airplanes MU-300 on February 24–27, 2016, and G-II on October 20–23, 2016. These two experiments were conducted to confirm the sounding rocket experiments and future international projects that will use sounding rockets.

3. Experimental procedure

The double wavelength Mach–Zehnder-type laser interferometer was re-designed to fit the limited sizes of MU-300 and G-II airplanes (**Fig. 1**). The components are similar to those used for ground experiments[8] and for sounding rockets[12]. The significant characteristics of the interferometer include tiny detectable differences of the order of 10^{-7}–10^{-6} the refractive index, the relatively wide view, and the simultaneous determination of temperature and concentration (partial pressure) of the evaporant by using two lasers: red (632.8 nm of He-Ne laser) and green (532 nm of semiconductor laser). The schematic image has been shown in **Fig. 2**.

The evaporation source was a filament with 0.2–0.3 mm φ in diameter connected between two electrodes 6 mm φ in diameter in the experimental chamber (**Fig. 2**). The evaporation source voltage and electron current were recorded. Temperature was measured by a pyrometer at the center of the evaporation source and by a Chromel–Alumel thermocouple at the end of the filament. All data was recorded by using a data logger including total pressure of the chamber and acceleration on a vibration control plate. For the airplane experiment, fixing of all experimental components and accessibility during the experiment must be established. We heavily modified the experimental system for a G-II airplane after the experiment using MU-300, because the interfaces of the two airplanes are different (**Fig. 1**).

For the microgravity experiment, we prepared the experimental setup completely one day prior to the flights except

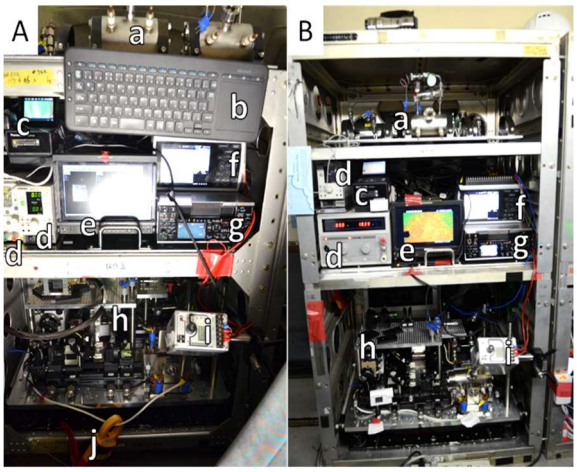

Fig. 1 Experimental system used to make a dust analog and for in situ observation of its formation processes. A: Double wavelength Mach–Zehnder-type laser interferometer on a vibration control device for MU-300 shown in February 2016. B: Same as, A but for G-II in October 2016. a: Chambers. b: keyboard with a mouse pad to operate a PC even under microgravity, if necessary. c: Recorder for high-resolution video camera. d: Stabilized power supply. e: Monitor for high-speed camera of Photron. f: Data logger. g: DV recorder for high-resolution video images with superimposed acceleration gravities. h: Main part of the double wavelength Mach–Zehnder-type laser interferometer. i: Pyrometer for measuring the temperature of the evaporation source inside the chamber. j: Ampere meter for measuring electron current to the evaporation source.

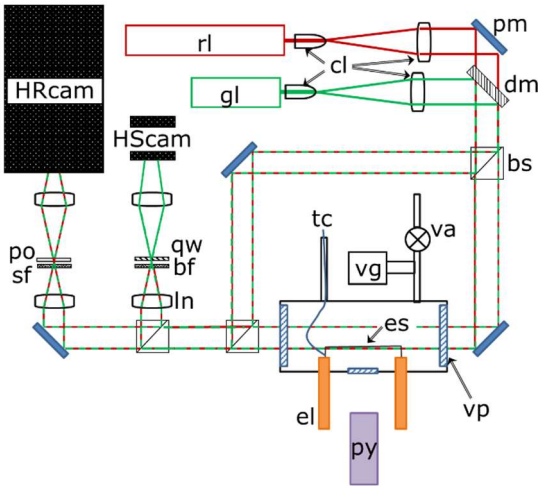

Fig. 2 Schematics of the experimental system. The configuration and optical path of the double wavelength Mach–Zehnder-type laser interferometer with a nucleation chamber corresponds to **Fig. 1** h. The red and green lines show the optical paths of the red and green lasers, respectively. The resulting images of interference fringes are recorded with a high-resolution video camera (HRcam) and a high-speed camera of Photron (HScam), which enables to record phase-shift interference fringes of green light due to allay polarizers on a detector device. Typical evaporation source is a tungsten filament 0.3 mm in diameter and 70 mm in length is shown as the black solid line (es) in the nucleation chamber. The other labels are as follows: bf: band pass filter. bs: beam splitter. cl: collimator. dm: dichroic mirror. el: electrode. ln: lens. pm: plate mirror. po: polarizer. sf: short-pass filter. tc: thermocouple. vg: vacuum gauge. gl: green laser. py: pyrometer. qw: quarter wavelength plate. rl: red laser. va: valve. vp: view port.

for making a final adjustment in the morning of the flight. The experimental chambers were evacuated down to lower than 10^{-4} Pa until as close as the flight time as possible (**Fig. 3**). Then, Ar gas was introduced into the chambers to reduce a mean free path of evaporated vapor; otherwise, the evaporated vapor sticks onto the wall of the chamber and forms a thin film instead of nanoparticles. The total pressure was controlled to be an order of 10^4 Pa to duplicate the formation process of dust around a dying star, which involves the relationship between the collision frequency of the growth units (atoms/molecules) and the timescale of supersaturation increase[2)].

All of the experimental systems powered on during a steady flight for 30 min to the airspace after departure from Nagoya airport. After arriving at the airspace and when the experiments were ready including other groups, the pilots began count down from 2 min. The gravity condition became approximately 2 G for MU-300 and 1.8 G for G-II airplanes, as shown in **Fig. 4A** and **B**, respectively, after the 30 s call (ii in **Fig. 4C**). After the 10 s call, the gravity became almost zero with a final call of "now" from a pilot and then we can receive a trigger signal from the airplane (iii in **Fig. 4C**). The averaged gravitational accelerations from "a

Fig. 3 Ground supporting systems. k: Movable ground pumping station composed of turbo molecular pump and oil-free scroll pump for evacuation of chambers and refilling with a gas. l: Ar and O_2 cylinders. m: Nitrogen-filled bench top for sample collection in O_2 and water vaporless conditions.

Table 1 Mean gravitational acceleration from a trigger signal to when the gravitational acceleration in the directions of the airplane ceiling starts to increase continuously in a microgravity corresponding to **Figs. 4A** and **B**. "all" means average data for all nine or twelve parabolas for a flight.

	Gx	*Gy*	*Gz*
A1	0.0065 ± 0.0039	0.0044 ± 0.0029	0.0137 ± 0.0097
A2	0.0050 ± 0.0028	0.0035 ± 0.0028	0.0090 ± 0.0080
A3	0.0050 ± 0.0029	0.0054 ± 0.0046	0.0146 ± 0.0121
A4	0.0063 ± 0.0031	0.0032 ± 0.0022	0.0102 ± 0.0103
A all	0.0059 ± 0.0034	0.0037 ± 0.0032	0.0128 ± 0.0112
B1	0.0068 ± 0.0041	0.0172 ± 0.0036	0.0192 ± 0.0314
B2	0.0075 ± 0.0051	0.0108 ± 0.0039	0.0198 ± 0.0154
B3	0.0058 ± 0.0033	0.0118 ± 0.0059	0.0196 ± 0.0129
B4	0.0049 ± 0.0036	0.0085 ± 0.0059	0.0129 ± 0.0105
B all	0.0059 ± 0.0044	0.0089 ± 0.0053	0.0168 ± 0.0165

trigger signal" to "when the gravitational acceleration in the directions of the airplane ceiling starts to increase continuously" for each axis and each flight have been summarized in **Table 1**. We performed experiments during the microgravity condition for 20 to 25 s of iii in **Fig. 4C**. The duration becomes longer in the opposing wind than in the following wind. Afterward, the gravitational acceleration became larger than the normal 1 G (typically ~1.6 G, iv in **Fig. 4C**) before the usual level flight at 1 G (i in **Fig. 4C**). **Figures 4A** and **B** show examples of the gravitational acceleration for two flights. Doable times for each flight experiment are 50 min for MU-300 and 60 min for G-II, respectively. Each experiment using MU-300 was completed within 3000 s from the first to the last parabolas as shown in **Fig. 4A**. Similarly, each experiment using G-II was completed within 3600 s as shown in **Fig. 4B**. Then allotted number of parabola is around 10 times for MU-300 and 12 times for G-II, respectively. If airplane reaches into a strong wind region or an experiment spent time for preparation after one parabola, we have to wait to fix the problem for next parabola like 2500-3000 s in A. **Figure 5** shows the focused data during microgravity conditions for the first two times corresponds to A and B in **Fig. 4**.

In each experiment, we exchanged the used experimental chamber for a new one, plugged a thermocouple plug and pressure gauge line into a data logger, and adjusted the focus of a pyrometer during the level flight of i in **Fig. 4C**. We mounted nine chambers for the experiment. Recording of high-vision camera images began at the 10 s call, and a trigger signal was sent to a high-speed camera for recording at the "now" call. After a few seconds, the evaporation source was heated by resistive heating and evaporated using a stabilizing power supply. An example temperature and pressure profiles corresponds to **Fig. 5A1** have been shown in **Fig. 6**.

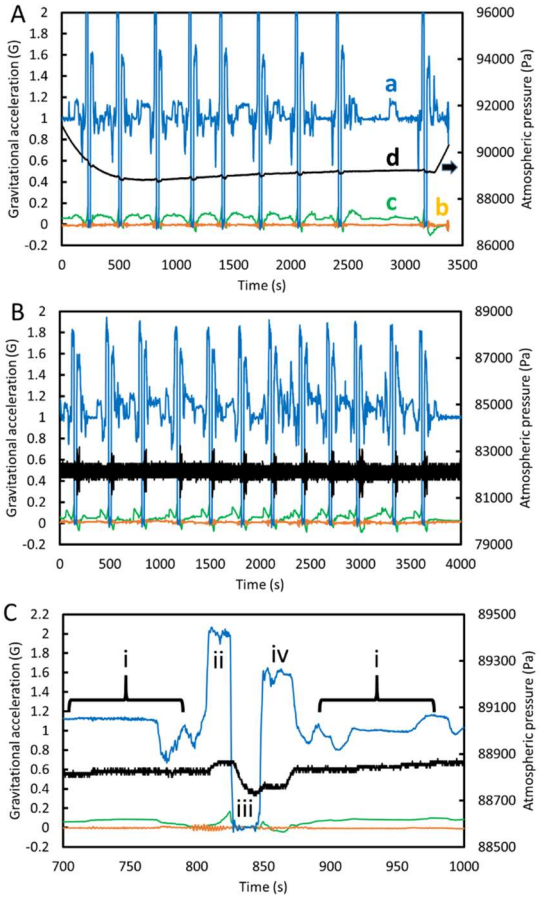

Fig. 4 Gravitational acceleration in the directions of the airplane ceiling (a, blue), right hand windows (b, orange) and nose (c green), and atmospheric pressure (d, black) during a flight. A: Datasets of a series of the flight using MU-300 on February 24, 2016. B: Datasets of a series of the flight using G-II on October 20, 2016. C: Gravitational acceleration in the direction of the airplane ceiling for first parabola in A. i: Steady state. ii: Pre-high G. iii: Microgravity. iv: Post gravity high G.

4. Experimental Results and Discussion

Figure 7 shows examples of time resolved images of interference fringes obtained at three different Ar gas pressures. The thickness of the donut-shaped smoke, which is composed of produced nanoparticles, just after nucleation depends on the total gas pressure of buffer Ar gas. In the case of lower gas pressure in **Fig. 7A2**, evaporated vapor can be diffused more efficiently owing to a longer mean free path than that in the higher gas atmosphere in **Figs. 7B2** and **C2**. The produced particles were distributed in almost all viewing areas of the laser in **Fig. 7A2**. In the case of larger gas pressure in **Fig. 7C**, slight changes in gravitational acceleration affected the movement of smoke owing to density differences in the gas warmed by a hot evaporation source. In the case of ideal microgravity conditions, the source

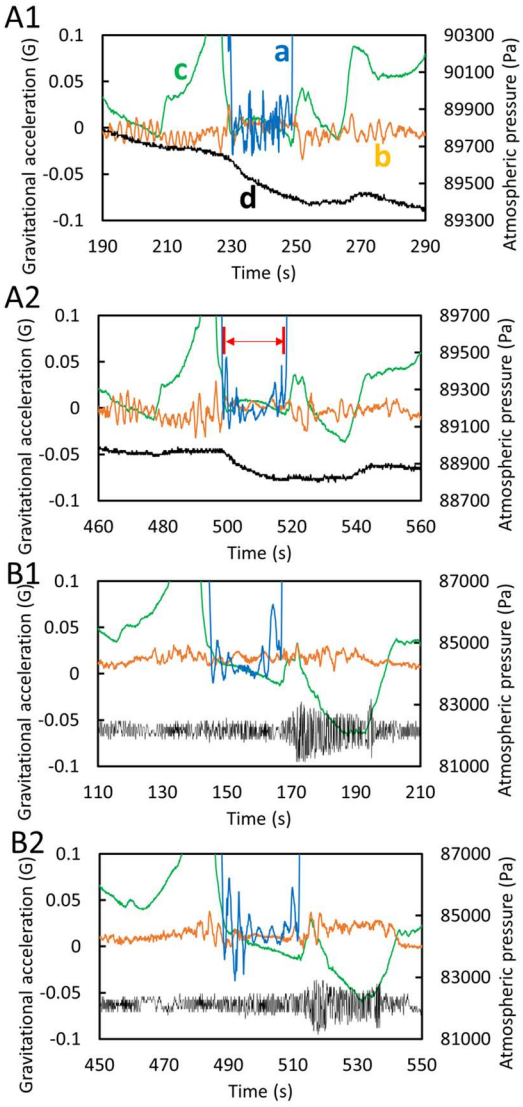

Fig. 5 Enlarged data of gravitational accelerations of first through two parabolas for each flight corresponds to **Figs. 4A** and **B**. For example, A1 and A2 correspond to first two parabolas in **Fig. 4A**. Gravitational acceleration in the directions of the airplane ceiling (a, blue), right hand windows (b, orange) and nose (c green), and atmospheric pressure (d, black) during a flight. Red arrow in A2 shows a region to obtain a mean value of gravitational acceleration.

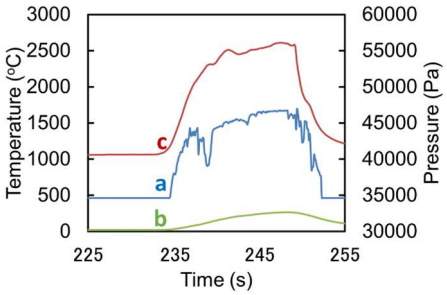

Fig. 6 An example of a dataset corresponds to **Fig. 5A1**. a, blue: Temperature measured by a pyrometer at the center of the evaporation source. b, green: Temperature by a Chromel–Alumel thermocouple at the end of the filament. c, red: Total pressure of the chamber.

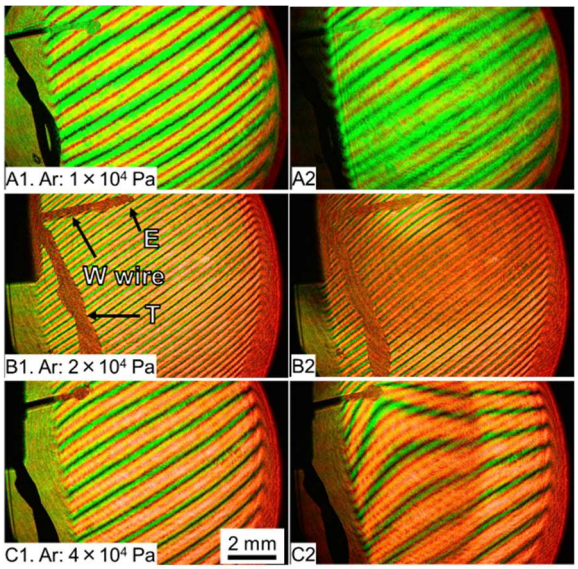

Fig. 7 Time resolved images of interference fringes for gold obtained at three different Ar gas pressures: A. 1×10^4 Pa, B. 2×10^4 Pa, and C. 4×10^4 Pa. "1" in the left column images were recorded before heating the evaporation source, and "2" in the right column images were recorded soon after nucleation. E is the evaporation source, and T is a Chromel–Alumel thermocouple.

material evaporates and diffuses concentrically, and nucleation then occurs homogeneously with the same distance from the evaporation source and produces nanoparticles that diffuse homogeneously even at higher gas pressures. The smoke in **Fig. 7C2** diffused faster in the direction of the bottom. This suggests negative gravity, which is in a direction opposite that of the usual rising current on Earth.

The effects of gravity can be easily recognized by comparing the shape of the smoke (**Fig. 8**). A hot evaporation source makes a strong convection current in a 1 G environment (**Fig. 8A**); therefore, cooler Ar gas always comes from the bottom of the evaporation source. Then, the evaporated vapor in the direction of the bottom rapidly cools and nucleates because of relatively larger supersaturation compared with that in other directions. In the case of microgravity, because the evaporated vapor cools more slowly, the timescale for supersaturation increase should be relatively longer, which is an advantage in mimicking the formation process of dust in a gas outflow of an evolved star[12,13].

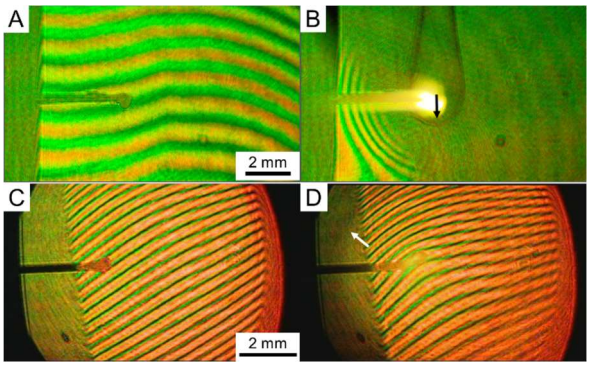

Fig. 8 Comparison of the shape of the produced iron smoke in Ar gas of 4×10^4 Pa between 1 G (A and B) and microgravity (C and D) environments with interference fringes. A and C are snapshots before heating. Arrows in B and D show smoke particles. For better visualization, parts of interference fringes have been disappeared by cutting the reference laser light.

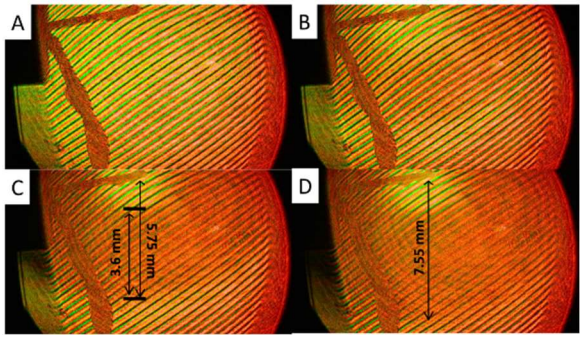

Fig. 9 Time resolved images of interference fringes for gold obtained in Ar gas pressure of 2×10^4 Pa. A to D correspond to 8.89, 9.55, 10.52, and 10.72 s after the trigger signal conveying entry to a microgravity environment. The thickness of the donut-shaped smoke became larger at a velocity of 3.6 mm s^{-1}.

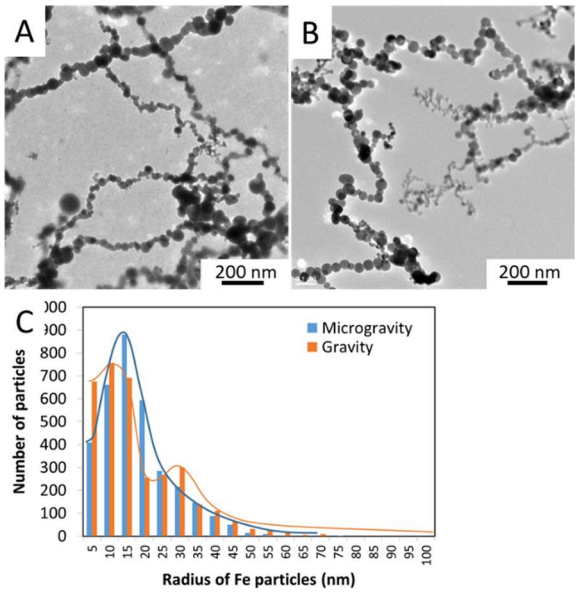

Fig. 10 Resulting Fe particles produced in Ar gas of 4×10^4 Pa. A: TEM image of Fe particles produced in gravity. B: TEM image of Fe particles produced in microgravity. C: Comparison of size distribution between 1 G (orange) and microgravity (blue). The two curves are given as a visual aid. The total number and mean diameters of the particles are 3354 and 15.3 nm for microgravity and 3313 and 15.5 nm for gravity (in the laboratory), respectively.

It is well known that supercooled liquid water in a bottle, which was not crystalized for a long time if we do not touch it, is immediately crystallized when shaken it. Density fluctuation may trigger the nucleation, although the exact reason why shock induces freezing of water is not understood. However, this phenomenon gives a simple hypothesis that the high-quality microgravity condition of a sounding rocket would suppress nucleation for long time if the nucleation from the vapor phase follows the same theorem. Reynolds number can be estimated by $Re = \frac{\rho v L}{\mu}$, where ρ is the density of the fluid, v is the velocity of the fluid with respect to the object, L is a characteristic linear dimension and μ is the dynamic viscosity of the fluid. Estimated *R*e of our experiments performed in Ar gas of 4×10^4 Pa are ~30 under gravity and ~0.3 under microgravity conditions, respectively, with assumptions of gas temperature at 1000 K, then, ρ = 0.2 kg·m^{-3}, v = 0.1 m·s^{-1} for gravity[14] and 0.3 m·s^{-1} for microgravity (**Fig. 9**), L = 0.07 m for the length of the evaporation source and $\mu = 5 \times 10^{-5}$ Pa·s^{-1}. In case of microgravity condition, the smaller *R*e value of 0.3 suggests that an effect of turbulence can be negligible. The *R*e value of 30 in a gravity condition seems also small compared with a transition value of 10^3 between laminar flow and turbulent flow. Nevertheless, we predict that tiny turbulence at the interface between evaporated vapor to the direction of the bottom of the evaporation source and Ar gas coming from the bottom, where relative velocity becomes larger, affect to a nucleation in a gravity condition. In other words, actual Reynolds number can be larger than 30 because of rapid diffusion of evaporated hot vapor against the convection of Ar gas. If turbulence is not the reason of the larger supersaturation and the size of a critical nuclei of Fe, which is only a single Fe atom in a microgravity condition using a rocket[12], we need to find other reason.

In the case of the microgravity experiment in Ar gas of 4×10^4 Pa using a sounding rocket, Fe nucleated 11 mm away from the evaporation source. In the airplane case, the distance was much shorter, at several millimeters in most cases. For example, Fe vapor nucleates ~2.5 mm from an evaporation source in an Ar gas of 4×10^4 Pa (**Fig. 8D**). This may be a result of density fluctuation owing to temporal fluctuation of gravity in the order of 10^{-2}–10^{-1} G, as shown in **Fig. 5** and **Table 1**. In the ground-based experiment under normal 1 G, nucleation occurred

in a much shorter distance of about 1 mm (**Fig. 8B**). These results also suggest that nucleation of the dust around a dying star may be affected by density fluctuation.

Turbulence and density fluctuation also induce collision of produced particles. In the case of nanoparticles, two nanoparticles can be immediately merged to become a single nanoparticle to decrease their total surface energy because the diffusion coefficient of the atoms is significantly larger than that of bulk materials[2]. Then, the number density, size, and size distribution will be changed from the homogeneously nucleated particle in gas convection. If we use this value, the sticking probability may be overestimated[9]. **Figure 10** shows transmission electron microscope (TEM) images and the size distribution of Fe particles produced in Ar gas of 4×10^4 Pa. In contrast with the monotonical size distribution of the produced particles in the microgravity environment, those made in the laboratory had a double peak. Nevertheless, the mean particle sizes were very similar, at 15.3 nm and 15.5 nm for particles produced in microgravity and in laboratory, respectively. The reason may be the abundant smaller particles, which form from the evaporated vapor in the upper direction of the evaporation source, in case of gravity condition. Because concentration of the evaporant is lower above the evaporation source than that below the evaporation source due to convection. The standard deviations were 9.7 and 12.5 nm for microgravity and gravity, respectively.

5. Summary

We summarized the experimental data obtained in this study under microgravity environments using an airplane and compared the results with those obtained under gravity in the laboratory. The major differences are the shape of the smoke and its diffusion velocity, size distribution of the resulting particles. Although the microgravity quality was not as good as that by sounding rocket, the possibility for further ex-situ analysis of the produced particles in terms of their size distribution, morphology, crystallinity and composition together with the repeatable experiments are highly beneficial in providing a strong supporting result to the experiment using a Japanese sounding rocket or future microgravity experiments using various flying objects. We are planning to conduct a future microgravity experiment using sounding rockets launched at White Sands Missile Range in New Mexico, USA, or Esrange, Sweden. The present results offer excellent starting data for determining the detailed future experimental conditions.

Acknowledgments

This work was partly supported by a Grant-in-Aid for Scientific Research (S) from KAKENHI (15H05731), Expert Committee for Space Environment Utilization Science, ISAS, JAXA and Joint Research Project supported by JSPS and MIZS under the Japan – Slovenia Research Cooperative Program.

References

1) A. Mnka, H. Pathak, S. Tanimura, J. Wölk, R. Strey and B.E. Wyslouzil: Phys. Chem. Chem. Phys., **14** (2012) 4505.
2) Y. Kimura and K. Tsukamoto: New perspectives on mineral nucleation and growth, From solution precursors to solid materials. eds. A.E.S. van Driessche, M. Kellermeier, L.G. Benning, D. Gebauer, Springer, (2017) p. 339.
3) J.J. De Yoreo, P.U.P.A. Gilbert, N.A.J.M. Sommerdijk, R.L. Penn, S. Whitelam, D. Joester, H. Zhang, J.D. Rimer, A. Navrotsky, J.F. Banfield, A.F. Wallace, F.M. Michel, F.C. Meldrum, H. Cölfen and P.M. Dove: Science, **349** (2015) 6760.
4) J. Lee, T. Tanaka and H. Mori: In situ atomic-scale observation of melting point suppression in nanometer-sized gold particles. Nanotechnology, **20** (2009) 475706.
5) P. Buffat and J.-P. Borel: Phys Rev A, At Mol. Opt. Phys., **13** (1976) 2287.
6) H. Yasuda, H. Mori, M. Komatsu, K. Takeda and H. Fujita: J. Electron Microsc., **41** (1992) 267.
7) Y. Kimura, Y. Saito, T. Nakada and C. Kaito: Physica E, **13** (2002) 11.
8) Y. Kimura, K.K. Tanaka, H. Miura, K. Tsukamoto: Cryst. Growth Des., **12** (2012) 3278.
9) Y. Kimura, H. Miura, K. Tsukamoto, C. Li, T. Maki: J. Cryst. Growth, **316** (2011) 196.
10) Y. Kimura, K. Murayama, T. Yamazaki and T. Maki: Prog. Crystal Growth Ch., **62** (2016) 400.
11) Y. Kimura and K. Tsukamoto: J. Jpn. Soc. Microgravity Appl., **28** (2011) S9.
12) Y. Kimura, K.K. Tanaka, T. Nozawa, S. Takeuchi and Y. Inatomi: Science Advances, **3** (2017) e1601992.
13) T. Yamamoto and H. Hasegawa: Prog. Theor. Phys., **58** (1977) 816.
14) S. Yatsuya, A. Yanagida, K. Yamauchi and K. Mihama: J. of Crystal Growth **70** (1984) 536.